Journal of Building Engineering 131 (2026) 117207

Contents lists available at ScienceDirect

Journal of Building Engineering

journal homepage: www.elsevier.com/locate/jobe

Experimental investigation on the seismic behavior and recoverability of a UHPC-based self-centering shear wall

Gao Ma [a,b,*], Guoxu Zhao [c], Hyeon-Jong Hwang [d,**]

[a] College of Civil Engineering, Hunan University, Changsha, 410082, China
[b] Key Laboratory for Damage Diagnosis of Engineering Structures of Hunan Province (Hunan University), Changsha, Hunan, 410082, China
[c] College of Civil Engineering, Hunan University, Changsha, 410082, China
[d] Department of Architecture and Architectural Engineering, Seoul National University, Seoul, 08826, Republic of Korea

ARTICLE INFO

Keywords:
Self-centering
Post-tension
UHPC
CFRP tendons
Shear wall
Recovery

ABSTRACT

Self-centering shear walls (SCSWs) have been extensively studied by many researchers with the aim of reducing damage and residual displacement after earthquakes. This paper proposes a type of SCSW, which can limit the post-earthquake damage of the SCSW to a certain area. In addition, the internal energy-dissipation steel bars of the shear wall can be replaced to quickly repair and strengthen the shear wall after earthquakes. The proposed shear wall uses ultra-high performance concrete (UHPC), which improves the crack resistance of the shear wall. Two SCSWs were fabricated, and post-tensioned steel tendons and CFRP tendons were used to achieve the self-centering ability. Cyclic loading tests were carried out, and the proposed SCSWs exhibited comparable seismic performance to the conventional shear wall. After the first cyclic loading test, the damaged components of the SCSWs were repaired and replaced. Cyclic loading test was again performed on the repaired SCSWs to evaluate the seismic performance, and it showed satisfactory seismic performance. The experimental study revealed that the proposed SCSWs were feasible, and could maintain the resilient even after strong earthquakes. additional, a new model was proposed to estimate the flexural strength of SCSWs and its accuracy was proved. Finally, a finite element analysis was conducted to simulate the mechanical performance of the specimens. The effects of tendons initial prestress, wall aspect ratio, and UHPC volume were systematically investigated.

1. Introduction

In order to solve the difficult problem of post-earthquake building repair, resilient structures have been widely studied [1–4]. Resilient structures can be normally used without repair or with low-cost repair after earthquakes [2]. The self-centering shear wall (SCSW) is one type of the resilient structures having self-centering ability to reduce deformation by itself and to avoid structural permanent damage under earthquakes. Compared to conventional shear walls, plastic deformation of SCSW is intentionally concentrated on a certain part of the component, and the residual deformation is controlled within a certain range through unbonded post-tensioned tendons.

* Corresponding author. College of Civil Engineering, Hunan University, Changsha, 410082, China.
** Corresponding author.
E-mail addresses: magao@hnu.edu.cn (G. Ma), zhaoguooxu@hnu.edu.cn (G. Zhao), hwanghj@snu.ac.kr (H.-J. Hwang).

https://doi.org/10.1016/j.jobe.2026.117207
Received 25 September 2025; Received in revised form 10 August 2026; Accepted 25 August 2026
Available online 28 August 2026
2352-7102/

The shear wall using unbonded post-tensioned tendons is the most typical self-centering shear wall (SCSW) structural system, which has been extensively studied and developed in the past two decades [2,5–9]. In the SCSWs, all or a part of longitudinal bars of the shear wall are not extended into the foundation. The structure can be restored to its original position through its self-weight and prestressing force of the tendons, generating a rocking mechanism to achieve self-centering [10,11].

Various studies revealed that rocking shear walls exhibited better self-centering and less damage than conventional monolithic shear walls [12–14]. However, the main problem of the SCSW structure lies in the weak connection between the wall and foundation, severe damage to the compression zone of the wall ends, difficulty in post-earthquake repair, and difficulty in repairing or replacing the energy dissipation steel bars after yielding [15–17].

Fiber reinforced polymer (FRP) materials have been widely used [18,19], and in this study, carbon fiber reinforced polymer (CFRP) bars were applied to shear walls to reduce residual displacement or increase self-centering capacity. Mohammad et al. [20] applied glass fiber reinforced polymer (GFRP) bars to SCSWs, and reported that SCSWs reduced the residual displacement and exhibited the energy dissipation and ductility levels comparable to those of conventional shear walls. However, use of FRP bars increased the crack opening at the wall-footing joint interface. According to Zhao et al. [21], use of FRP bars significantly reduces the residual displacement of the wall, but the energy dissipation capacity decreases. Despite high-strength and linear elastic behavior of FRP bars, research on its use as tendon reinforcement to provide self-centering forces is relatively limited. Use of FRP bars for the self-resetting bars in SCSW does not require prestressing force, which can leverage the linear elasticity advantages.

In existing studies, unbonded post-tensioned bars (or tendons) were designed to remain elastic to enable self-centering, while energy dissipating devices were designed to undergo inelastic deformation and provide energy dissipation under cyclic loading. Zhang et al. [22] developed a resilient hinge device installed at the wall corner. Compared with the conventional wall, the proposed self-centering shear wall decreased wallboard damage, and improved the energy dissipation capacity and deformation capacity. Liu et al. [23] proposed a new kind of replaceable energy dissipation component installed at the bottom corner of reinforced concrete (RC) walls, which significantly improved the seismic performance. Wang and Zhu [24] proposed a self-centering RC shear wall system enabled by super elastic shape memory alloy bars to achieve self-centering. However, as very long shape memory alloy bars are buried in concrete, it is not convenient to repair and replace the damaged bars later. Although the internal energy dissipation devices have been proved to be efficient to improve the energy dissipation capacity of SCSWs, the devices are not easy to replace after yielding under strong earthquakes.

Ultra-high performance concrete (UHPC) has ultra-high strength, good ductility, and excellent durability [25–27], which has been widely applied in beams, columns, shear walls, and bridge systems [28–32]. To mitigate damage at the corners of the section of SCSW, UHPC has been adopted at the corners of the shear wall. Sharma et al. [33] used UHPC in the boundary elements of the retrofitted walls and provided additional confinement to reduce damage at the rocking corners. Replacing normal concrete at the rocking corners with UHPC eliminated damage at the rocking corners, which decreased the requirement of confinements hoops. Li et al. [34] utilized steel-confined UHPC in the plastic hinge region of self-centering columns to mitigate damage at the plastic hinge under earthquakes.

In general, plastic deformation is concentrated by the concrete crushing and longitudinal bar yielding at the corner of the wall section. At the compression zone of the wall section, closely-spaced transverse reinforcements are used for concrete confinement, which improves the deformation capacity. Post-tensioned of tendons restores the structure to its original position for self-centering,

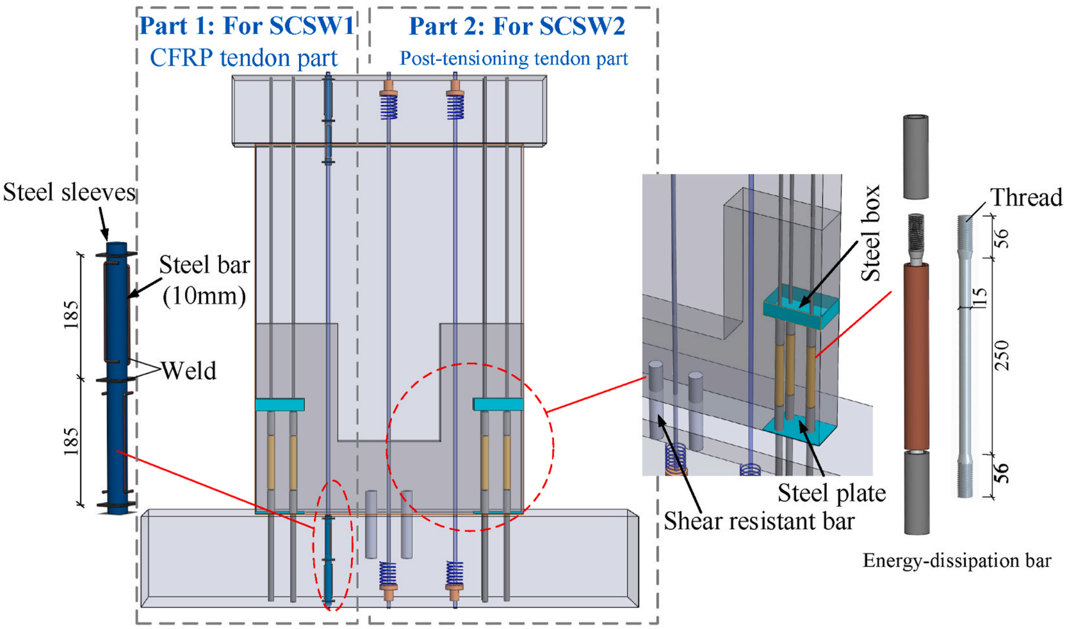

Fig. 1. Configurations of self-centering shear wall with resilient hinge devices (unit: mm).

which reduces the residual deformation of the structure [35–37]. Although extensive research has been performed on self-centering shear walls, prestressing tendons, and UHPC materials respectively, few efforts have been devoted to integrating replaceable energy-dissipators, local UHPC reinforcement and CFRP prestressing tendons within one shear-wall system. Moreover, cyclic loading tests involving repair and reloading operations for such composite components are still rarely reported. This provides the primary research motivation for the present study.

This study presents two SCSW designs. UHPC is applied to mitigate damage at the wall base and deliver enhanced compressive and tensile restoring forces. Energy-dissipation bars are employed to provide seismic energy-dissipation capacity for the shear wall. Moreover, CFRP tendons are incorporated into the SCSW specimens to evaluate their self-centering performance. The proposed SCSW specimens are repaired after the first-cycle loading test and retested subsequently, aiming to explore the feasibility of the adopted seismic-resilient design concepts.

2. Test plan

2.1. Details of wall specimens

Fig. 1 shows the configuration of the SCSW specimens. The reinforcement detailing of the SCSW specimens was designed based on the test conditions and conventional concrete shear wall specimens from previous studies [38]. The geometric scaling ratio between the fabricated specimens and the practical prototype shear walls ranges from 1:2 to 1:1.5. The test parameters were the self-centering details (i.e., SCSW1 using post-tensioned tendons, SCSW2 using CFRP tendons, and conventional shear wall SW0), and retrofitting (i.e., SCSW1-R and SCSW2-R retrofitted from SCSW1 and SCSW2, respectively).

All the specimens consisted of three parts: loading beam, wall, and foundation beam. Fig. 2 shows the details of the two SCSW specimens. The height, width, and thickness of the wall are (1650, 1200, and 140) mm, respectively. At both sides of the wall section, boundary element of the width of 200 mm was adopted to prevent early concrete crushing under cyclic loading. The dimensions of the loading beam and foundation beam were (250 × 300 × 1400) mm and (400 × 450 × 2200) mm, respectively.

The post-tensioned tendons, energy-dissipation steel bars, UHPC, and shear-dissipation bars were used at the bottom of the wall. Unlike the conventional shear wall, longitudinal bars were not extended into the foundation in SCSW specimens. In specimens SCSW1 and SCSW2, post-tensioned tendons and CFRP tendons were used at the middle region of the wall section, respectively. Part 1 of Fig. 1 illustrates the anchorage detail of CFRP tendons in SCSW2, which are anchored through the steel sleeves filled with reactive powder concrete in the loading beam and foundation beam. Part 2 of Fig. 1 illustrates the anchorage detail of post-tensioned tendons in SCSW1,

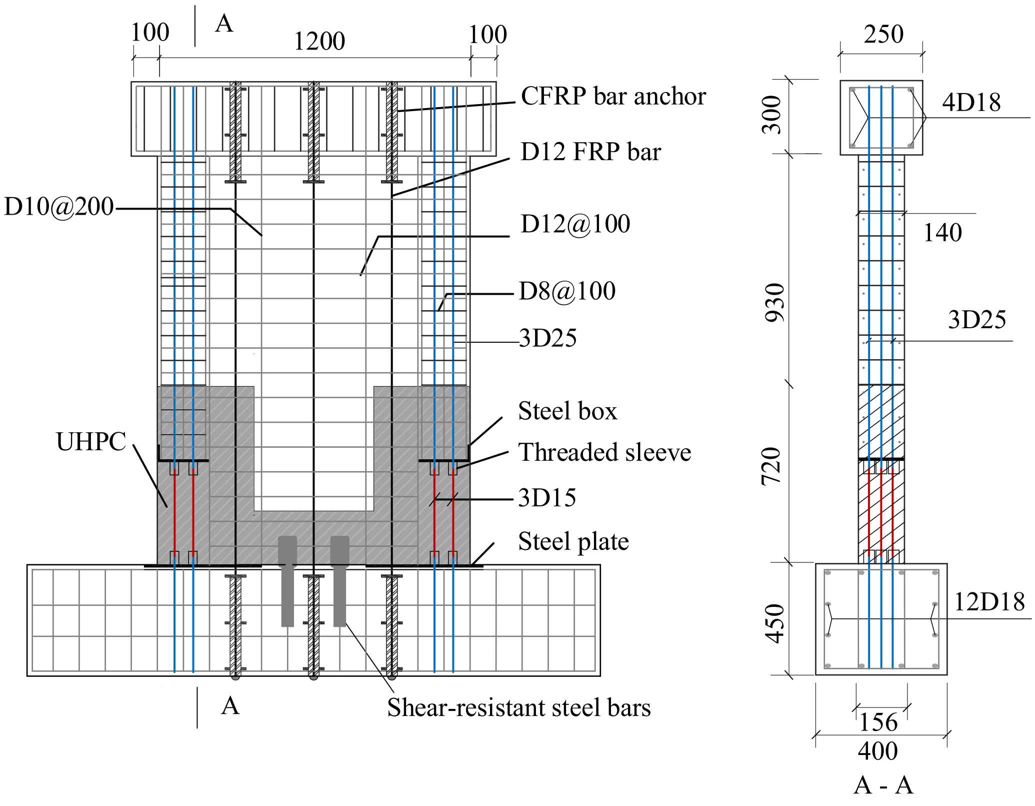

Fig. 2. Details of wall specimens (unit: mm).

which are anchored through steel anchors.

Three energy-dissipation steel bars were placed at the both sides of the wall section. Steel threads were used to connect the steel bars with the pre-embedded steel bars in the special boundary elements. After connecting the energy-dissipation steel bars, UHPC was poured into the U-shaped area at the bottom of the SCSWs. For separation of UHPC in the expected damage region of the special boundary elements, steel plates and steel boxes were installed at the both ends of the energy-dissipation steel bars. This construction configuration prevents damage to the foundation beam and the upper region of the expected damage region at the special boundary element, ensuring that the primary damage is concentrated in the replaceable region (i.e., expected damage region) for easier repair after damage. Additionally, shear-resistant steel bars with 40 mm diameter were placed between the shear wall and foundation beam to prevent shear sliding failure of the wall.

In the wall web, D10 bars (i.e., diameter of 10 mm) were distributed at spacings of 100 mm and 200 mm in horizontal and vertical directions, respectively. In the special boundary element, D8 bars (i.e., diameter of 8 mm) were used for stirrups at a spacing of 100 mm. Three D25 bars were embedded in the special boundary element (except the expected damage region) and foundation beam at each side of the wall section, and three D15 energy-dissipation bars (i.e., diameter of 15 mm) were arranged at the expected damage region in a triangle pattern with a spacing of 100 mm among them. The replaceable energy dissipating bars and pre-embedded D25 bars were connected by tightening the threaded sleeves onto the rebars. This approach also facilitates post-earthquake repairs. The replaceable energy-dissipation bars were covered by steel sleeves with the length of 105 mm, outer diameter of 32 mm, and thickness of 4 mm, to prevent buckling of the energy-dissipation bars.

Three high-strength steel tendons with a diameter of 15.2 mm were used in the wall web of specimen SCSW1. The cross-sectional area of each tendon was 140 mm^2. Specimen SCSW2 used three CFRP tendons with the diameter of 12 mm and cross-sectional area of 113 mm^2. Note that after shear wall was installed, post-tensioned force was applied by 52 kN(0.2 yield stress) to each steel tendon, while prestressing force was not applied to CFRP tendons.

For design of a SCSW, it is necessary to consider both the self-centering capacity and energy dissipation capacity of the wall. The moment contribution ratio can reflect the relative magnitude of the self-centering and energy dissipation capacities of the SCSWs, which is defined as follows [39]:

$$\lambda = \left(M_{\mathrm{pt}} + M_{\mathrm{N}}\right) / M_{\mathrm{s}} \tag{1}$$

where λ is the moment contribution ratio; M_{pt} is the moment capacity developed by the prestressing force; M_{N} is the moment capacity developed by the axial force; and M_{s} is the moment capacity developed by the energy-dissipation bars. M_{pt}, M_{N}, and M_{s} can be calculated with aspect to the centroid of the concrete compression resultant of the section.

According to Palermo et al. [40], when the moment contribution ratio λ ranges from 1.15 to 1.25, the "flag shaped" hysteresis curve of the self-centering shear walls can be obtained. ACI ITG-5.1 [41] provides a standard for ensuring the self-centering ability of structures, in which the flexural resistant capacity contributed by the energy-dissipation steel bars does not exceed 40% of the total flexural bearing capacity of the wall. In Eq. (1), the flexural contribution of energy-dissipation steel bars in specimen SCSW1 was calculated to be 38% when the diameter of the energy dissipation bars was 15 mm.

2.2. Materials properties

Table 1 shows the basic mechanical properties of the rebars, post-tensioned steel tendons, and CFRP tendons used in SCSW. The material properties were same as SW0 and obtained from the tensile test results of three rebars at each type according to GB/T 228.1-2021 [42].

C30 concrete were used for the loading beam and wall body. C50 concrete was used for the foundation beam to prevent the deformation or damage. The compressive strengths of normal concrete and UHPC were measured by three C30 concrete cubes with size of (150 × 150 × 150) mm and three UHPC cubes with size of (100 × 100 × 100) mm, respectively. The average compressive strengths of C30 concrete and UHPC were (34.1 and 124.4) MPa, respectively. The cube strengths of C30 concrete and UHPC can be converted to standard cylinder strengths of (23.9 and 110.7) MPa, respectively [43,44].

Table 1
Geometric and material properties of reinforcement.

Reinforcement	Type	Diameter, d_{b} (mm)	Yield strength, f_{y} (MPa)	Tensile strength, f_{u} (MPa)	Modulus of elasticity E (GPa)
HPB300	Stirrup	8	376.0	470.0	200
HRB400	Vertical distribution rebar	10	461.3	599.0	200
	Horizontal distribution rebar	10	473.5	619.5	200
	Energy dissipation rebar	15	444.7	598.7	200
Steel tendon	——	15.2	1797	1898.7	200
CFRP tendon	——	12	——	2507.7	161

3. Test setup

3.1. Loading program

Fig. 4 shows the test setup. The foundation beam of the wall specimen is fixed on the ground through the compression beam and ground anchor. The loading beam is connected to the 1000 kN actuator with the displacement range of ±250 mm.

Before the test, a 20% axial force (i.e., 462 kN) of the design axial load was applied [45]. For cyclic lateral loading, displacement-controlled loading was applied according to ACI 374.2R-13 (ACI 2013) [46] and ACI ITG-5.1-07 (ACI 2008) [41]. Three load cycles were applied at every drift ratio θ of (0.20, 0.25, 0.35, 0.50, 0.75, 1.00, 1.50, 2.00, 2.50, 3.0, and 3.50)%. The schematic diagram of loading protocol can be seen in Fig. 5. The drift ratio (θ) was defined as the ratio of the lateral displacement (δ) to the distance between the lateral loading center and the top surface of the foundation. According to specification GB 50011-2010 [45], when the wall specimens reach the drift ratio (θ_{lim}) of 2%, severe damage is considered to be occurred, and the test can be terminated. Nevertheless, the proposed shear walls have better deformation capacity than conventional shear walls. Existing studies on similar self-centering wall systems commonly adopt target drift ratios ranging from 2.0% to 3.0% for cyclic loading testing [47–49]. Therefore, further loading can be performed in light of actual test conditions. After the SCSW is repaired, the test is terminated once the shear wall reaches failure.

3.2. Test measurements

In order to draw out the lead wire conveniently, the strain gauges of the post-tensioned steel tendons and CFRP tendons are pasted on the ends. Fig. 6 shows the locations of strain gauges and displacement gauges. The strain gauges at the replaceable energy-dissipation bars of the specimens are labeled as A1~A6 to measure its tensile and compressive strains, the strain gauges at the steel tendons or CFRP tendons are labeled as A7~A12, and the strain gauges at the horizontally distributed bars are labeled as H1~H3.

Fig. 6(b) shows 13 linear variable different transformers (LVDTs) installed in the wall. Six LVDTs (W1~W6) along the height of the wall were used to measure the variations of the curvature of the wall. Two LVDTs (W7 and W8) were used to measure the gap between the wall and foundation beam. LVDT W9 was used to measure the horizontal sliding displacement of the wall. Two LVDTs W12 and W13 were used to measure the shear deformation of the wall.

3.3. Post-earthquake repairing of the damaged wall specimens

The primary concept of the design is expected to facilitate post-earthquake repair. The concrete and energy-dissipation steel bars in the corner regions of shear wall section would be damaged after earthquakes, which require maintenance and repair.

Fig. 3 shows the repair process of the damaged wall specimens. After the first cyclic loading test, the damaged UHPC and tension bars at the compression zone (i.e., intended replaceable region) are completely removed (Fig. 3(a)). After clearing the replacement area (Fig. 3(b)), the damaged energy-dissipation bars are disassembled. Threaded nuts are installed on the lower segments of the 25 mm-diameter rebars. The failed energy-dissipation bars are unscrewed from the nuts, and new energy-dissipation bars assembled with connecting sleeves are then screwed back to their original installation positions. Then, the transverse bars and concrete are replaced (Fig. 3(c) and (d)). Damaged UHPC can be removed by electric pickaxes, and threaded energy-dissipation bars allow direct screw-in replacement within limited on-site space without extensive structural demolition, achieving favorable construction convenience.

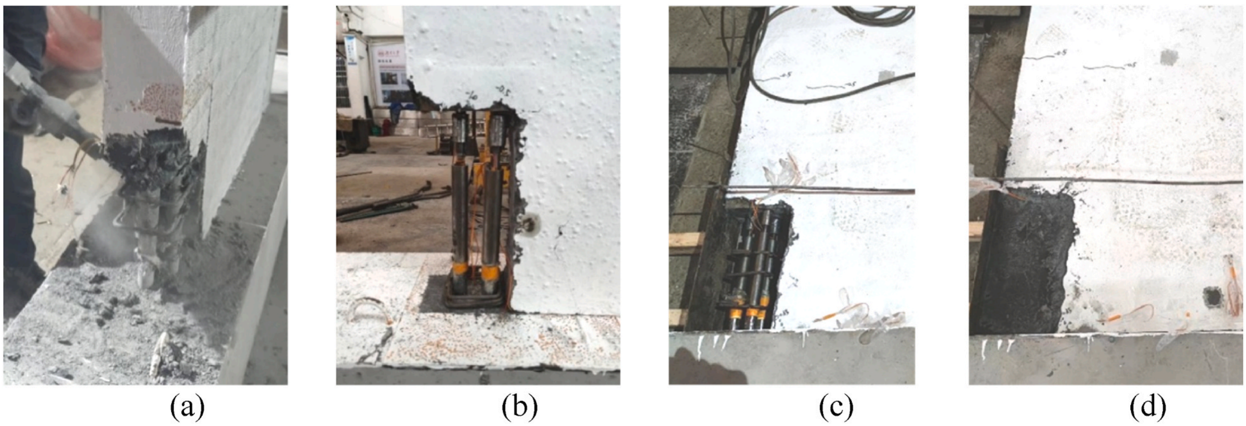

Fig. 3. Repair process of the damaged wall specimen: (a) removal of UHPC in the replaceable region; (b) replacement of the energy dissipation bars; (c) replacement of stirrups; (d) curing of UHPC concrete.

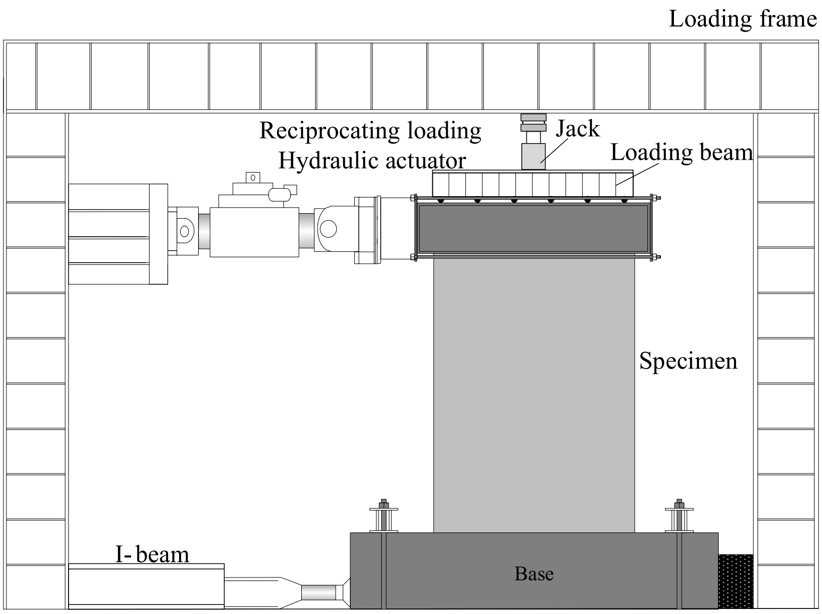

Fig. 4. The schematic drawing of test setup.

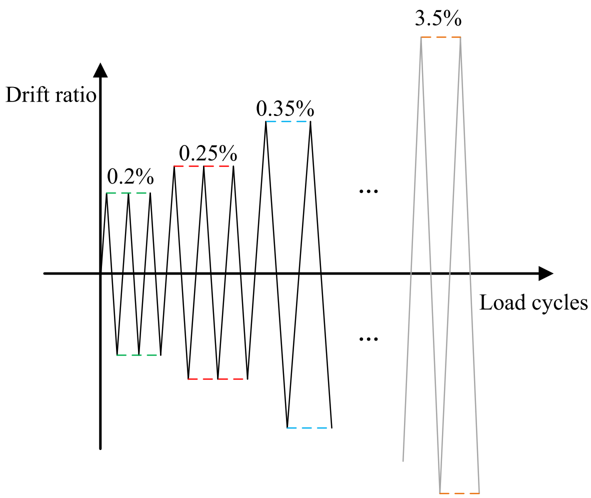

Fig. 5. Schematic diagram of loading protocol.

4. Test results

4.1. Damage and failure mode

Fig. 7 shows the local failure modes of test specimens. In specimen SCSW1, cracking and separation of UHPC in the replaceable region occurred when the drift ratio (θ) reached 0.27% (Fig. 7(a)). As seen in Fig. 7(b), at $\theta = 0.55\%$, a diagonal crack with a width of 0.9 mm developed at UHPC region in the corner region of the wall. At $\theta = 1.1\%$, horizontal cracks appeared at the interface between the replaceable UHPC region and steel box on the left side of the wall, and the rocking mechanism was fully developed. On the other hand, no further cracks appeared in the wall body. Ultimately, at $\theta = 2.8\%$, the post-tensioned steel tendons were still elastic, and the damage of UHPC was insignificant (Fig. 7(c)). According to GB 50011-2010 [45], because the drift ratio exceeded θ_{lim}, the test was terminated without significant strength degradation. As the damage is concentrated at the replaceable region, the damaged wall can be conveniently repaired.

Cyclic behavior of SCSW2 was similar to that of SCSW1. This is because the both specimens have similar test parameters, except for the details of post-tensioned reinforcement. This result implies that utilizing CFRP tendons for SCSWs is feasible. Compared to conventional shear walls, SCSWs exhibited fewer noticeable cracks and damage, demonstrating better seismic performance.

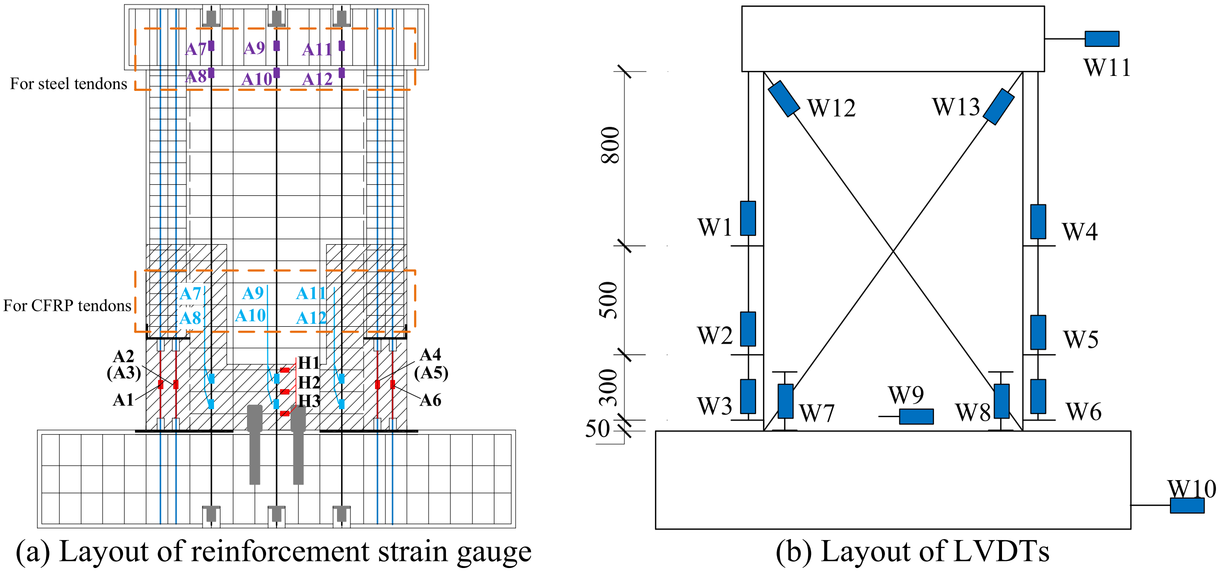

Fig. 6. Locations of strain gauges and LVDTs (unit: mm).

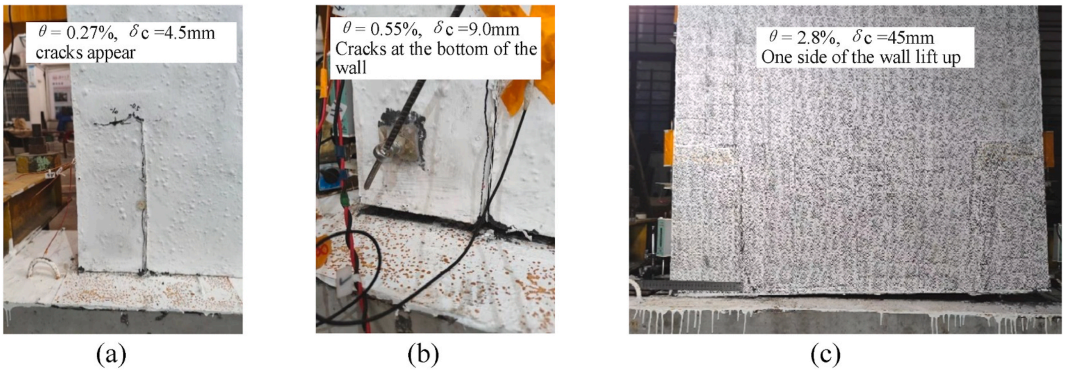

Fig. 7. Local failure modes of SCSW1.

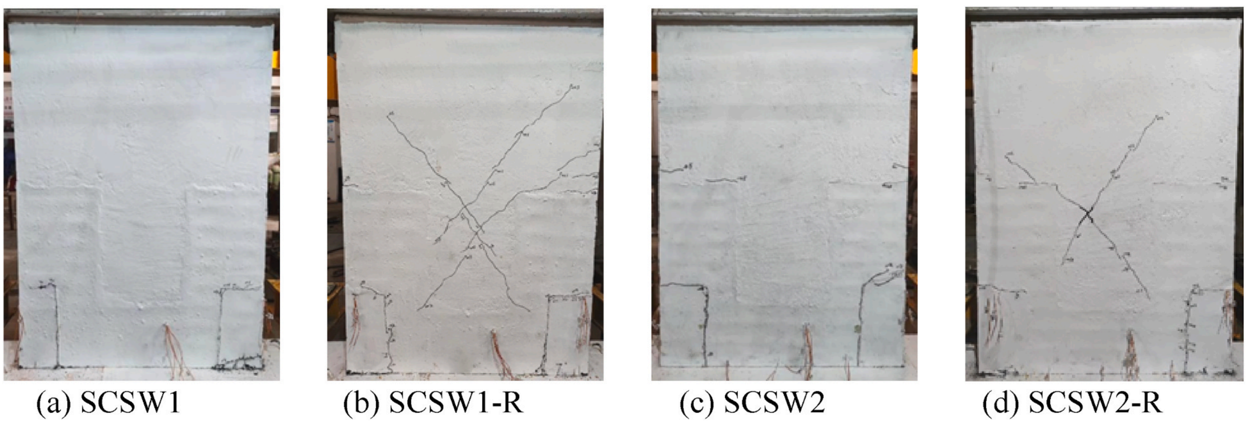

Fig. 8. Failure modes of the specimens at the end of tests.

SCSWs exhibited a notably different failure mode from conventional monolithic RC shear wall SW0 [38]. At a drift ratio of 2.0%, SW0 developed dense X-shaped diagonal shear cracks across the wall panel, with severe concrete crushing-spalling at its base and damage propagating over the full wall height. By contrast, SCSW damage concentrated on lifted wall toes and horizontal interfaces between cast-separated components, and wall-panel cracking remained much slighter. Such differences in damage patterns are attributed to three factors including rocking deformation, post-tension-induced sectional pre-compression, and concentrated energy dissipation at the base joint.

The hysteretic behavior and failure mode of specimens SCSW1-R and SCSW2-R under reloading process after repair were similar to those of the original specimens. Compared to the first cyclic loading test, under the second cyclic loading, diagonal shear cracks appeared at low drift ratio in the wall body due to pre-damage. The failure mode of the specimens is shown in Fig. 8. In SCSW2-R, during reloading, diagonal cracks appeared on the wall, and the test was stopped when the load decreased to 80%. At the point of failure, one side of the CFRP reinforcement fractured, and some replaceable energy-dissipating steel reinforcement sleeves were pulled out.

4.2. Lateral load–drift relationship

Fig. 9 shows the lateral load (P) – drift ratio (θ) relationships of specimens SCSW1, SCSW2, and SW0. In SCSW1, at the initial loading state, hysteresis curve was in the elastic phase, and the residual displacement was negligible (Fig. 9(a)). At $\theta = 0.82\%$, lateral stiffness decreased due to yielding of the replaceable energy-dissipation bars. After $\theta = 0.82\%$, inelastic behavior increased, showing large energy dissipation capacity. The overall hysteresis curve exhibited the minimal residual displacement. At the end of loading, the load-carrying capacity did not decrease, and the maximum load ($P_{max} = 521.55$ kN) occurred approximately at $\theta = 2.75\%$.

In SCSW2, the hysteretic behavior was similar to that of SCSW1 (Fig. 9(b)). SCSW2 exhibited relatively larger stiffness and no residual displacement before $\theta = 0.38\%$. After $\theta = 0.38\%$, the lateral stiffness decreased, and inelastic behavior occurred. The maximum load was 521.00 kN at $\theta = 2.75\%$. Compared to SCSW1, SCSW2 accumulated higher energy dissipation. This is attributed to the smaller stiffness and residual displacements in SCSW1, which result in a reduced hysteresis loop area. The stiffness of SCSW2 is higher than that of SCSW1, the reason is that there are 370 mm anchoring ends at both ends of CFRP tendons, so the free expansion range of CFRP tendons is smaller and the overall stiffness of SCSW2 is larger.

Compared to SW0, both SCSW specimens SCSW1 and SCSW2 exhibited lower initial stiffness (approximately 80% of that of SW0), because there have no connections between walls and foundations. However, unlike SW0 showing strength degradation, the load-carrying capacity of SCSWs continuously increased after yielding of the replaceable energy-dissipation bars due to the elastic behavior of steel or CFRP tendons. Further, SCSW1 and SCSW2 effectively controlled the damage and residual deformation. These characteristics make SCSWs attractive options for improving the seismic resilience of structures.

Fig. 10 compares the cyclic curves of the repaired specimens SCSW1-R and SCSW2-R under reloading. At $\theta = 0.61\%$, a plateau occurred in the cyclic curve of the repaired specimens due to yielding of rebars at the first test. Compared to the original specimens (i.e., the peak load = 521.55 kN for SCSW1 and 521.00 kN for SCSW2), the load-carrying capacity of the corresponding repaired specimens decreased to 497.35 kN for SCSW1-R and 503.45 kN for SCSW2-R. This is because the damaged wall concrete at the first cyclic loading was not completely repaired. Further, due to a certain degree of slip of the threaded sleeve during the repair process, the energy-dissipation bars connecting sleeve was pulled out at large drift, which decreased the load-carrying capacity at negative 60 mm displacement. Pinching behavior also occurred in the repaired specimens. The residual displacement of the repaired specimens was the same as that of the original specimens at each load cycle. In a word, the proposed SCSW could still achieve satisfactory seismic performance after post-earthquake reinforcement and repair.

The yield drift ratio (θ_y) was defined based on the equivalent elasto-plastic system with secant stiffness at 75% of P_{max}. The ultimate drift ratio (θ_u) was defined as the post-peak point of 80% of P_{max} [50,51]. The ductility (μ) was defined as the ratio of the ultimate drift ratio to yield drift ratio.

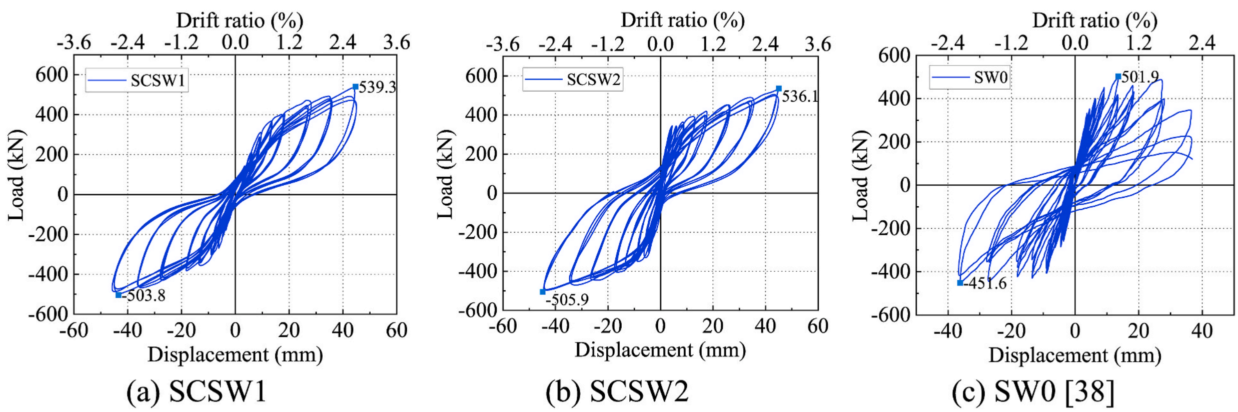

Fig. 9. Hysteretic curves of the specimens.

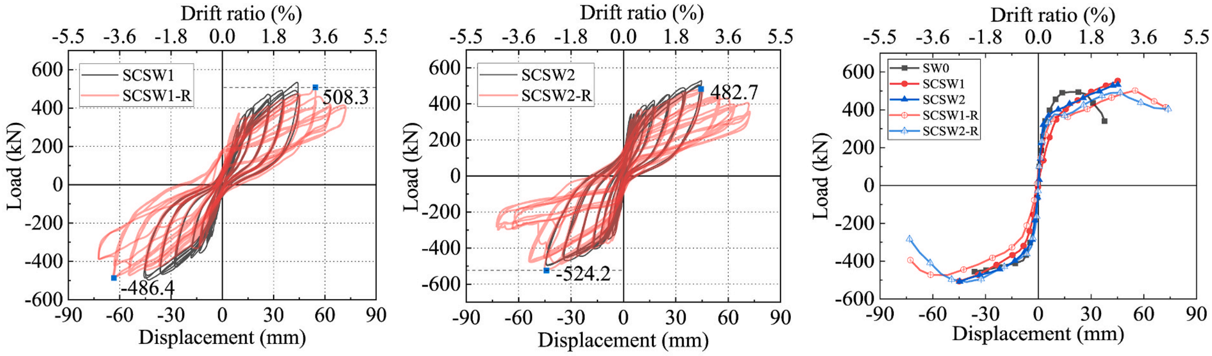

(a) SCW1 and SCW1-R (b) SCW2 and SCW2-R (c) Skeleton curves of the specimens.

Fig. 10. Hysteretic and skeleton curves of the specimens.

Table 2
Deformation capacities of specimens.

No.	P_{max} (kN)	θ_y (%)	θ_u (%)	μ
SCSW1	521.55	0.53	2.73	5.19
SCSW2	521.00	0.25	2.73	11.04
SW0	476.75	0.46	1.98	4.33
SCSW1-R	497.35	0.58	4.20	7.21
SCSW2-R	503.45	0.34	4.02	11.67

Notes: P_{max} denotes the average value of the two the peak load of the specimen; θ_y is the yield drift ratio, if the skeleton curve does not have a yield point, take the yield drift ratio of the steel bar; θ_u is the ultimate drift ratio; μ is the ductility; which can be calculated by $\mu = \theta_y/\theta_u$.

In Table 2, the average maximum load of specimens SCSW1 and SCSW2 was (7.6 and 6.8)% greater than that of SW0, respectively. The average ductility of SCSW1 and SCSW2 was (20 and 155)% greater than that of specimen SW0, respectively. The ductility of SCSW2 was 2.13 times that of SCSW1 due to larger yield drift in SCSW1.

4.3. Residual displacement

By controlling residual displacement, it is possible to achieve structural self-centering. In this study, the relative residual displacement R_{res} was used to measure the magnitude of the residual displacement of wall specimens (refer to Eq. (2)).

$$R_{res} = \frac{|\Delta_{ri}^{+}| + |\Delta_{ri}^{-}|}{|\Delta_{i}^{+}| + |\Delta_{i}^{-}|} \tag{2}$$

where Δ_{ri}^{+} and Δ_{ri}^{-} indicate the residual displacements after each load cycle in the positive and negative loading directions, respectively.

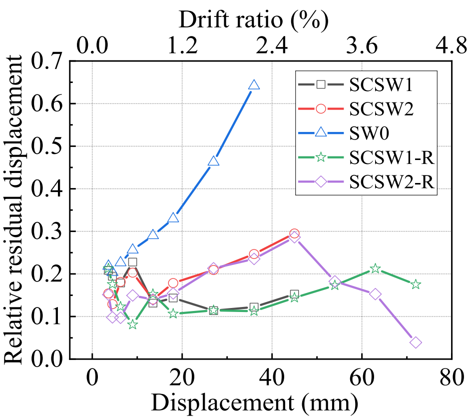

Fig. 11. Residual displacement of test specimens.

The relative residual displacements for each test specimen are shown in Fig. 11. Both specimens SCSW1 and SCSW2 maintained the relative residual displacement, which was significantly less than that of specimen SW0 showing continuous increase of the residual displacement. The maximum residual displacement of SCSW1 and SCSW2 decreased by (76.2 and 54.0)%, respectively, compared to SW0. This reduction was attributed to the self-centering force of post-tensioned steel tendons and CFRP tendons. After the energy-dissipation bars yielded, the residual displacement occurred. However, as the lateral drift increased, the high-strength and linear elastic properties of the steel tendons and CFRP tendons were fully utilized, which demonstrated the excellent self-centering effect on the controlling of the residual displacement. Compared with SCSW2, SCSW1 generally produces smaller residual displacement, and its residual drift reaches approximately 50% of that of SCSW2 within the drift ratio range of 1.2% to 2.4%. This is because the initial prestressing of the steel tendons in SCSW1 restrained the excessive residual deformation resulted from free length of the steel tendons in SCSW1 is greater than that of SCSW2, which allows for greater deformation. The repaired specimens showed the residual displacements similar to the counterpart initial specimens until the strength degradation. At drift of 2.7% for SCSW1-R and 3.8% for SCSW2-R, the bearing capacity of the specimens degraded. The connecting sleeves of the replaceable energy-dissipation bars were pulled out, which eliminated the energy-dissipation capacity and thereby produced a prominent reduction in the residual displacement ratio.

4.4. *Energy dissipation capacity*

Fig. 13 compares the cumulative energy dissipation capacity of wall specimens. The cumulative energy dissipation capacity was calculated by accumulating an enclosed cyclic curve of each load cycle at each drift ratio. The cumulative energy dissipation capacity of specimen SCSW2 was a little greater than that of specimen SCSW1 because of smaller initial stiffness and residual displacement of SCSW1. The cumulative energy dissipation capacity of SCSW1 and SCSW2 with rebar ratio of 1.9% was (34.3 and 22.1)% less than that of SW0 with rebar ratio of 2.4%, because of the requirement limitation of replaceable energy-dissipation bar ratio for self-centering in SCSW1 and SCSW2 (refer to Eq. (1)). Meanwhile, in accordance with *Code for Seismic Design of Buildings* [45], the energy dissipation capacity of the specimens is further evaluated using the equivalent viscous damping ratio ζ_{eq}, which is calculated as follows:

$$\zeta_{\mathrm{eq}} = \frac{1}{2\pi} \cdot \frac{S_{\mathrm{ABD}} + S_{\mathrm{BCD}}}{S_{\Delta\mathrm{AFO}} + S_{\Delta\mathrm{OCE}}} \tag{3}$$

where $S_{\mathrm{ABD}} + S_{\mathrm{BCD}}$ represents the area enclosed by the hysteresis loop, and $S_{\Delta\mathrm{ABD}} + S_{\Delta\mathrm{BCD}}$ denotes the sum of the areas ΔAFO and ΔOCE, as illustrated in Fig. 12.

In the repaired specimens SCSW1-R and SCSW2-R, the cumulative energy dissipation capacity decreased a little because of the damaged rebars and concrete and the reduced load-carrying capacity. At the early stage of loading, the equivalent viscous damping ratios of specimens SCSW1 and SCSW2 were higher than that of SW0. In specimens SCSW1 and SCSW2, uplift occurred at the base of the wall, and energy dissipation was primarily concentrated in the replaceable tensile-side energy-dissipating reinforcement. As the displacement increased, the damage to specimen SW0 intensified, resulting in increased energy dissipation. Consequently, its equivalent viscous damping ratio rose rapidly and eventually surpassed those of SCSW1 and SCSW2. Due to prestress in the steel strands of SCSW1, the plastic deformation of the replaceable energy-dissipating reinforcement is smaller than in SCSW2. The prestress also suppresses tensile stress, preventing cracking in the SCSW1 UHPC and concrete, reducing energy dissipation capacity.

4.5. *Strain of rebars and tendons*

4.5.1. *Replaceable energy-dissipation bars*

Fig. 14 shows the variations of the maximum strain of the replaceable energy-dissipation steel bars in accordance with the lateral drift. Strain gauges A1, A3, and A6 in SCSW1-R and A4 in SCSW2-R collected no data due to test error. The energy-dissipation bars were mainly in tension, while the compressive strain of the energy consuming steel bars was relatively small. In SCSW1, the rebar

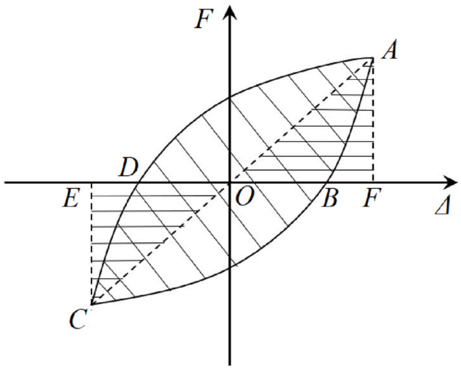

Fig. 12. Illustration of the equivalent viscous damping ratio calculation.

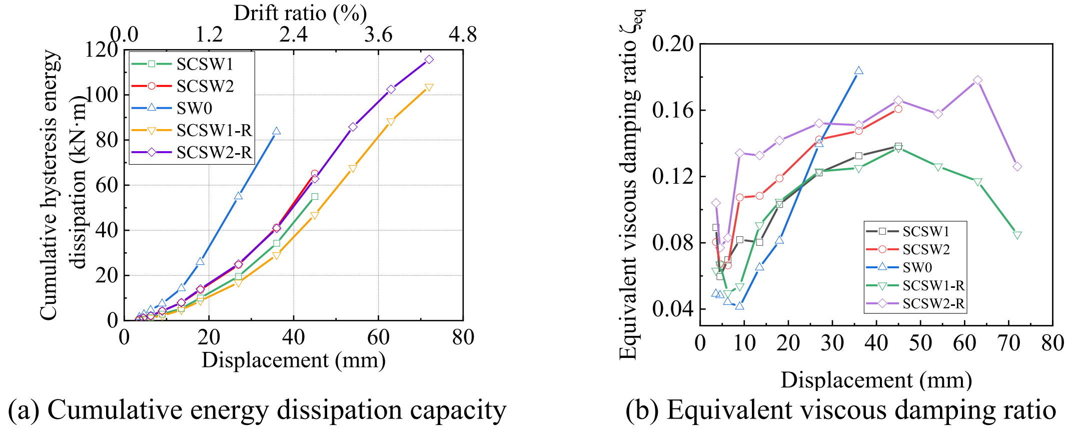

Fig. 13. Energy dissipation capacity of test specimens.

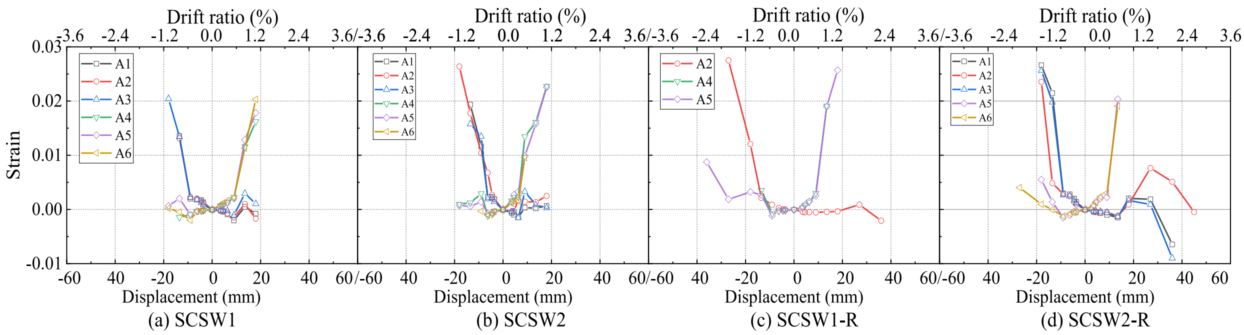

Fig. 14. Strain of replaceable energy-dissipation bars.

strain increased rapidly after the drift ratio (θ) exceeded 0.55% due to tensile yielding of the rebar. In contrast, for SCSW2, a sudden change in tensile strain of the rebar occurred after $\theta = 0.28\%$. This result indicates that the application of prestressing force on the energy-dissipation bars induces compression, which effectively delays the rebar yielding. When the drift ratio θ reaches 1.2%, the edge-located energy-dissipation bars have mostly yielded, so that it is necessary to repair these energy-dissipation bars after the test. After repair, SCSW1-R and SCSW2-R showed the similar rebar strain development to the counterpart initial specimens.

4.5.2. *Web horizontal rebars*

Fig. 15 shows the variations of the maximum strain of the web horizontal rebars in accordance with the lateral drift. The compression of the steel reinforcement here is due to the strain gauge being located between two shear resistant steel bars. The maximum strain of 186.9 με for SCSW1 and 94.3 με for SCSW2 was less than the yield strain (=2.3 × 10^3 με) due to no critical shear failure, indicating that SCSW1 experienced greater shear deformation than SCSW2. It can also be seen that the shear deformation is mainly concentrated at the bottom of the shear wall.

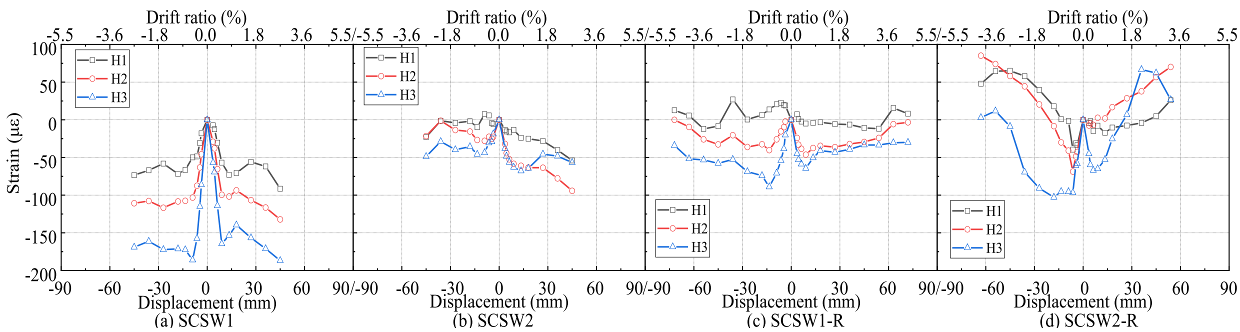

Fig. 15. Strain of web horizontal rebars.

In SCSW1, the strain of the web horizontal rebars was maintained after $\theta = 0.55\%$, because the overall deformation was governed by flexural behavior due to the noticeable uplifting of the wall bottom. In SCSW2, the strain of the web horizontal rebars is small. In the repaired specimens SCSW1-R and SCSW2-R, the horizontal rebars strains differed from those of the counterpart initial specimens due to concrete damage, the compression between steel bars decreases or tension occurs.

4.5.3. Post-tensioned steel tendons and CFRP tendons

Fig. 16 shows the variations of the maximum strain of the steel tendons and CFRP tendons in accordance with the lateral drift. Because the strain gauges on the post-tensioned steel tendons in specimen SCSW1 were entirely damaged after the initial loading, the strain conditions under reloading after repair were not documented. The tensile strain of the steel tendons in SCSW1 was less than that of the corresponding CFRP tendons in SCSW2. This is because 1) the unbounded length of the CFRP tendons is shorter than those of the steel tendons due to the grouting sleeve with a length of 370 mm at each end of the CFRP tendons, and 2) early yielding of the replaceable energy-dissipation bars in SCSW2. After unloading or negative loading, the steel tendons in compression zone decreased with the increase of displacement. On the other hand, in specimens SCSW2 and SCSW2-R, early yielding of the energy-dissipation bars and large plastic deformation developed the tensile strain of CFRP bars in compression zone.

4.6. Deformation

The overall deformation of shear wall specimens is contributed by the sum of flexural deformation, shear deformation, and sliding deformation (refer to the section of "3.2 Test measurements"). The contribution of shear deformation of the wall to the overall displacement can be calculated as follows:

$$\Delta_s = \frac{d}{2b}(\delta_{s2} - \delta_{s1}) \tag{4}$$

where Δ_s is the shear displacement; δ_{s1} and δ_{s2} are the diagonal displacement measurement (refer to W12 and W13 in Fig. 6(b)); d is the diagonal length of the wall; and b is the width of the wall.

The contribution of flexural deformation of the wall can be calculated with Eq. (5):

$$\Delta_f = \frac{H}{2b}(\delta_{f2} - \delta_{f1}) \tag{5}$$

where Δ_f is the flexural displacement; δ_{f1} and δ_{f2} are sum of W1~W3 and W7, and W4~W6 and W8, respectively; and H is the height of the wall.

Fig. 17 compares the contribution of each deformation to the lateral drift in test specimens. Overall, the lateral drift was dominated by the flexural deformation. Compared to SW0, shear deformation was significantly decreased in SCSW1 and SCSW2. At $\theta = 2.7$, the shear deformation contribution was (5.3 and 3.8)% in SCSW1 and SCSW2, respectively, while SW0 exhibited larger shear deformation contribution of 20.1%. This result implies that the degree of damage to SCSW1 and SCSW2 is smaller than that of SW0, as the connection between the wall and foundation in SCSW1 and SCSW2 is weaker. Consequently, the bottom of the shear wall on the tension side was separated from the foundation as the lateral drift increased, and the wall panel was primarily deformed through flexural mechanism, showing the minimal shear deformation. Despite pre-damage of concrete in the repaired specimens, the difference of the deformation contributions between the initial and repaired specimens was insignificant.

The flexural displacement of the wall mainly includes the uplift displacement at the bottom of the wall and the flexural deformation at the middle height. Fig. 18 shows the ratio of the uplift displacement to the displacement at each location. As seen in Fig. 18(a)~(c), due to the weak connection between the wall and foundation, the flexural deformation of specimens SCSW1 and SCSW2 was governed

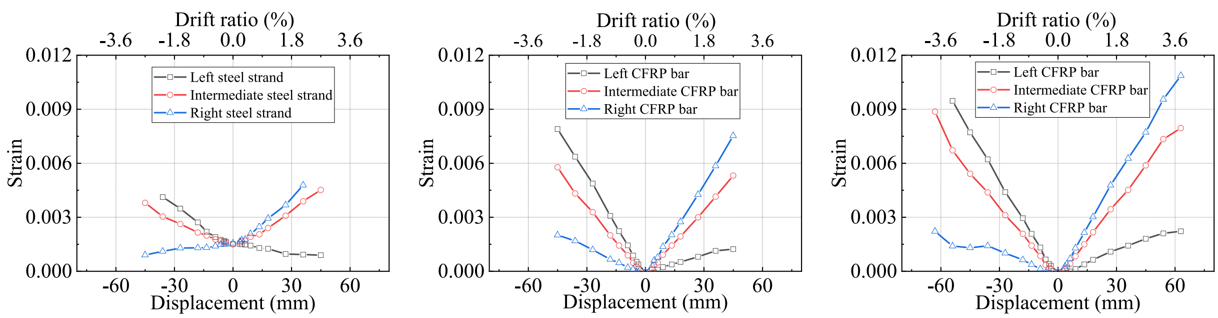

(a) Strain of post-tensioned tendons in specimen SCSW1. (b) Strain of CFRP tendons in specimen SCSW2. (c) Strain of CFRP tendons in specimen SCSW2-R.

Fig. 16. Strain of steel tendons and CFRP tendons.

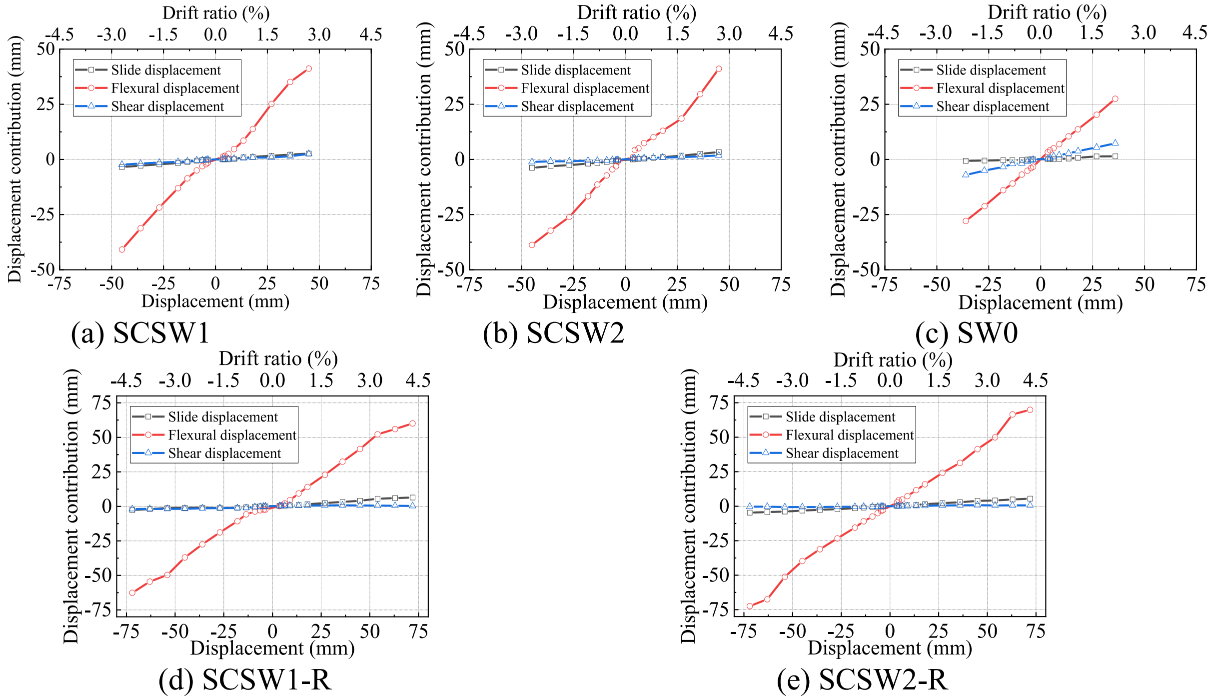

Fig. 17. Comparison of displacement contributions in test specimens.

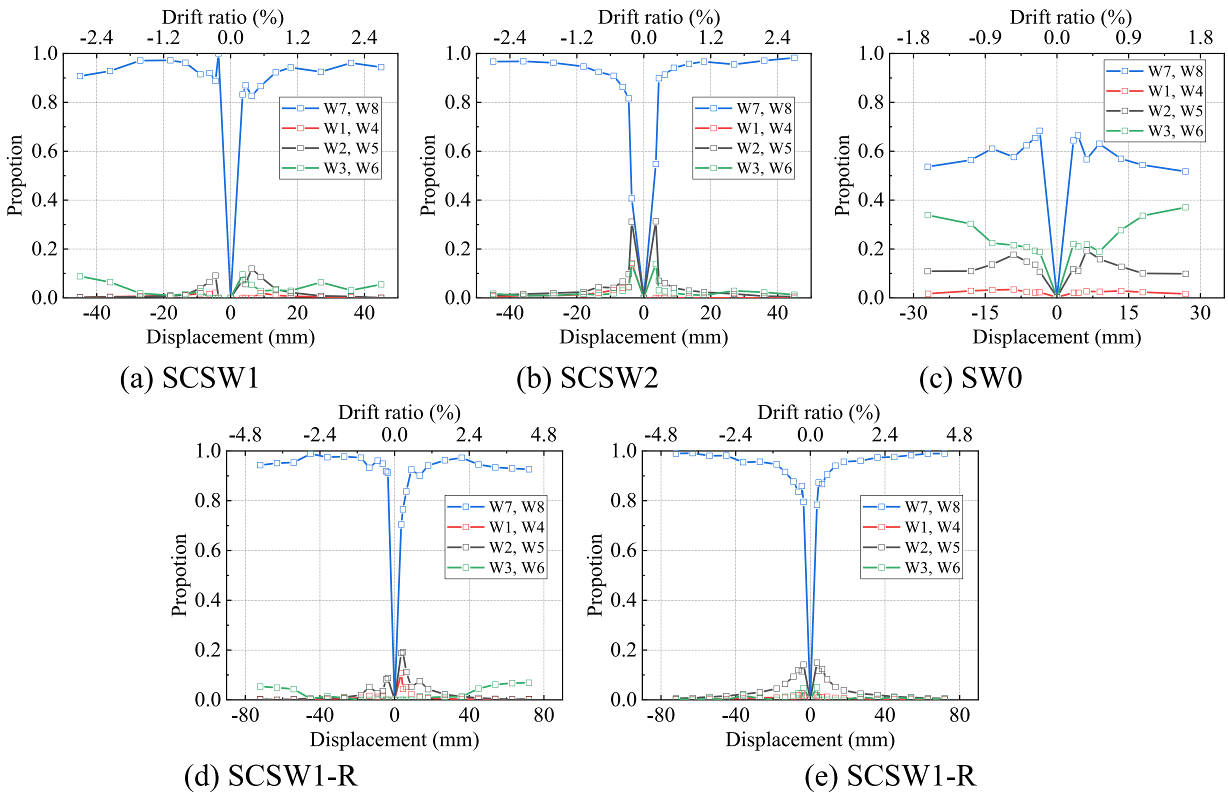

Fig. 18. Proportion of the flexural displacement.

by the uplift displacement of the wall (i.e., W7 and W8), which was larger than that of SW0. The repaired specimens exhibited the similar flexural deformation to the counterpart initial specimens (Fig. 18(d) and (e)). When the uplift displacement is large, self-centering mechanism is easily developed, and the wall damage is relatively reduced, which facilitates the post-earthquake structural repair.

5. Prediction of flexural strength of SCSW

5.1. Description of the flexural strength model

Due to the self-centering capability and strong deformation capacity of the shear walls, neither of the walls experienced shear failure at the end of the test. Thus, this study focused on the prediction of flexural resistance of the proposed SCSW. The following assumptions are considered to estimate the flexural strength: 1) On the basis of the test results, when the wall panel is detached from the foundation, overall flexural deformation is assumed to be developed by the gap between the wall panel and foundation (i.e., the slight flexural deformation of the wall panel is neglected); 2) Assuming a rigid body motion of the wall panel, shear sliding deformation of SCSW is negligible. and there is a certain width of the compression zone at the corner of the wall and the reason can be seen in Fig. 7 (c); and 3) For simple calculations, only the replaceable energy-dissipation bars and steel tendons (or CFRP tendons) are considered for longitudinal reinforcement. Further, the maximum stress in all reinforcements remains below the yield stress.

In the proposed SCSW, the moment equilibrium condition can be derived from the idealized force distribution of longitudinal reinforcement, as shown in Fig. 19.

$$\sum M_i = \sum f_i \cdot l_i = 0 \tag{6}$$

where M_i is the sum of all moments developed by longitudinal reinforcement at point O; f_i is the force of longitudinal reinforcement, and l_i is the lever arms of the corresponding f_i from point O.

Eq. (6) can also be expressed as follows:

$$F \cdot H = f_{ps}A_{ps}\left(d_{ps} - \frac{c}{2}\right) + f_{ed}A_{ed}\left(d_{ed} - \frac{c}{2}\right) + N\left(\frac{l_w}{2} - \frac{c}{2}\right) \tag{7}$$

where (f_{ps} and f_{ed}) and (d_{ps} and d_{ed}) are the stress of post-tensioned tendons and energy-dissipation bars and the corresponding length to wall corner, respectively; A_{ps} and A_{ed} are the cross-sectional area of post-tensioned tendons and energy-dissipation bars, respectively; N is the axial load on the wall section; c is compressive zone length; and l_w is the wall length.

The stress for each post-tensioned tendon can be calculated as follows [52]:

$$f_{psi} = f_{sei} + L_{pl}(\varepsilon_{cu} - \varepsilon_0)\left(\frac{d_i}{c} - 1\right)\frac{E_{ps}}{l_{ps}} \tag{8}$$

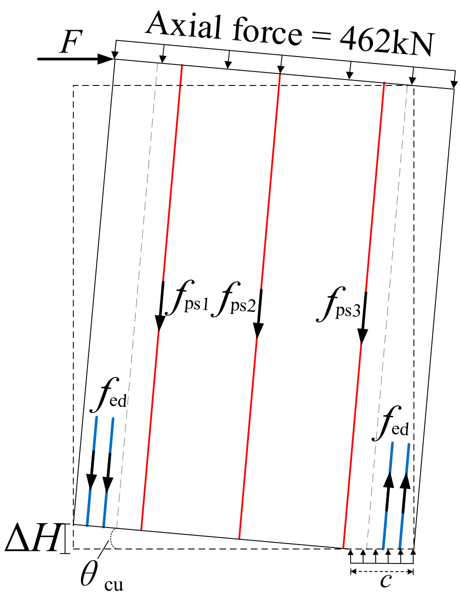

Fig. 19. Idealized force distribution of the test specimen.

$$f_{\mathrm{c}} = \frac{\sum f_{\mathrm{sei}} A_{\mathrm{psi}} + N}{l_{\mathrm{w}} b_{\mathrm{w}}} \tag{9}$$

where f_{sei} is the initial effect stress of post-tensioned tendons; L_{pl} is the plastic henge length of shear wall ($=0.11 l_{\mathrm{w}} + 3475 \frac{f_{\mathrm{c}}}{f'_{\mathrm{c}}}$ (mm)); f'_{c} is the concrete compressive strength; f_{c} is the axial stress of the wall section (Eq. (9)); b_{w} is the shear wall width; l_{ps} is the unbonded length of the post-tensioned tendons; E_{ps} is the elastic modulus of the longitudinal reinforcement; d_i is the cross-sectional area of the longitudinal reinforcement; and ε_0 is the strain at decompression point (Eq. (10)).

$$\varepsilon_0 = \frac{2\left(\sum f_{\mathrm{sei}} A_{\mathrm{psi}} + N\right)}{l_{\mathrm{w}} b_{\mathrm{w}} E_{\mathrm{c}}} \tag{10}$$

where E_{c} is the concrete elastic modulus.

The equivalent compressive zone length (c) can be determined according to force balance condition.

$$c = \frac{\sum f_{\mathrm{psi}} A_{\mathrm{psi}} + N}{\alpha \beta f'_{\mathrm{c}} b_{\mathrm{w}}} \tag{11}$$

where α and β are the equivalent stress block parameters; and $\alpha\beta$ can be taken as 0.85.

By combining Eq. (8) and Eq. (11), the length of the compression zone during bending failure can be obtained. The flexural capacity of the shear wall can be calculated from Eq. (6).

5.2. Validation and discussion

Firstly, the flexural-strength of the proposed self-centering shear wall is predicted. At limit rotation (θ_{cu}), the flexural strength of SCSW1 and SCSW2 was calculated as (477.7 and 567.6.0) kN, respectively, which was 6-8% less than the test results (508.3 and 524.40 kN). The predicted values are very close to the experimental values; however, the errors would be attributed to inaccurate prediction of plastic hinge length for UHPC. Next, to verify the validity of the proposed method, 44 sets of experimental data from the literature were collected [2,8,12,53–55]. The collected data have a height-to-width ratio ranging from 1.1 to 3.3, with lengths (l_{w}) and heights ranging from 1000 to 2000 mm and 2200~4000 mm, respectively. The number of steel strands ranges from 1 to 5, with an area ranging from 176.7 to 883.5 mm^2, and concrete strength ranging from 25.8 to 45 MPa. For easy demonstration, a comparison was made using shear force under flexural strength. The predicted results are shown in Fig. 20 and evaluated by three indexes: the *mean*, standard deviation (*SD*), and root mean squared error (*RMSE*) of the ratio of predictions to tests. From Fig. 9, it can be seen that the predictions closely matched with the test results, showing the *mean* value of 1.13, *SD* value of 0.15 and *RMSE* value of 0.20. It should be noted that this method is applicable only to rocking shear walls with high rigidity.

6. Finite element analysis

6.1. Finite element model

Fig. 21 shows the finite element method (FEM) models of specimens SCSW1 and SCSW2. Concrete is modeled using the C3D8R solid element, with the concrete damage plasticity model [56] employed as the constitutive model (Fig. 22). The constitutive model of UHPC is consistent with that in reference [57]. CFRP is defined as a linearly elastic material, and failure occurs once its ultimate strain is reached. Reinforcing bars are represented by T3D2 truss elements. Specifically, the rebars are embedded within the concrete. Owing to the rocking-dominated deformation of the wall during testing, flexural deformation remains small, and the bond-slip effect between reinforcement and concrete is neglected. The steel rebars are embedded into concrete via the “embed” constraint. The energy-dissipation bars are connected with reinforcements by “tie” connection, without any bond relationship with UHPC. bottom surfaces of the foundation beams are fully restrained, while the loading beams are constrained to prevent out-of-plane displacement. The interface between the UHPC wall and normal concrete is connected using tie constraint. As seen in the test results, both specimens SCSW1 and SCSW2 exhibited uplift at the base of the wall. For this reason, the bond effect between the precast foundation beam and UHPC was disregarded. The interface between the UHPC and foundation beam was modeled using the surface-to-surface contact approach. The tensile and compressive constitutive behavior of concrete was defined according to GB 50010-2010 [56]. A "hard" contact model was applied to allow the transfer of compressive stress. The finite-element model adopted the same displacement-controlled cyclic loading protocol as the test. Solid concrete parts employed a mesh size of 70 mm for critical zones and 150 mm for other regions. Additionally, the ends of the steel strands were constrained using infinitely modulus spring elements to simulate end anchorage. Zero-friction contact was defined between steel strands and concrete, and the prestressing stress σ was applied using the cooling method to apply an initial stress of 0.2 times the strand yield stress (i.e., $0.2 f_{\mathrm{py}}$).

$$\sigma = \alpha T E \tag{12}$$

where α is the length reduction factor per unit temperature; T is the cooling temperature; and E is the elastic modulus of post-tensioned tension. Note that the prestress loss is not considered in this study.

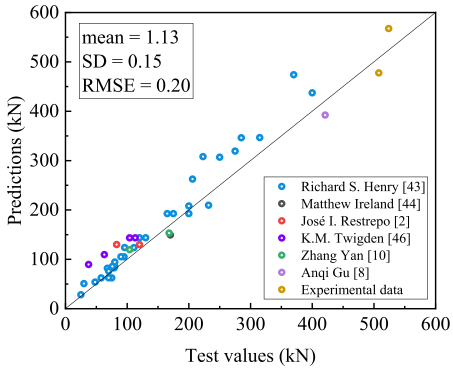

Fig. 20. Comparison shear force at flexural strength.

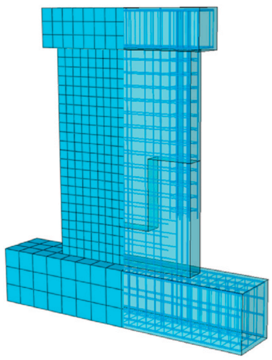

Fig. 21. Element modeling of the shear wall specimens.

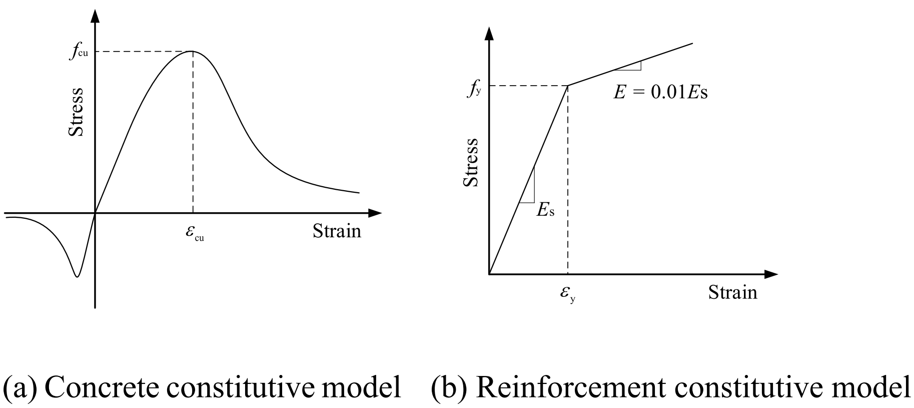

Fig. 22. Material constitutive models.

6.2. Model validation

According to GB 50011-2010 [45], the termination condition for quasi-static tests of unbonded prestressed shear wall structures is exceeding the maximum drift ratio limit of 2.0%. When the displacement reaches 45 mm (consistent with the experiment), the drift ratio is 2.7%, which can be considered as the termination condition for the test. The load-displacement curves of specimens SCSW1 and SCSW2 obtained from the FEM analysis were compared with the test results (Fig. 23). The analysis curves exhibited a similar trend to the experimental curves. The differences between the analysis and experimental results remain within an acceptable range. However, the FEM model did not account for the bond-slip effect between the rebars and concrete, and the manufacturing imperfections and gaps, which would result in an overestimated initial stiffness. Table 3 shows that the predicted load at each displacement closely

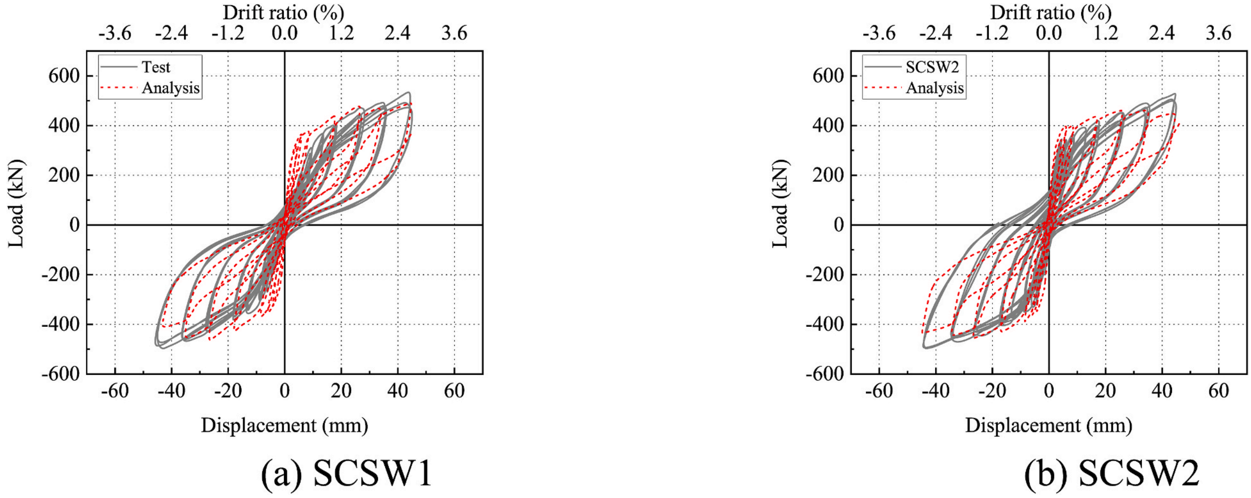

Fig. 23. Comparison between the FEM analysis and test result in the lateral load–displacement curves.

Table 3
Comparison of analysis and test results.

Specimen	$f_{1.5,s}$ (kN)	$f_{1.5,t}$ (kN)	*ERR* (%)	$f_{2.7,s}$ (kN)	$f_{2.7,t}$ (kN)	*ERR* (%)
SCSW1	467.9	444.4	5.3	483.6	490.4	1.4
SCSW2	456.9	432.8	5.6	444.6	495.7	10.3

Note: $f_{1.5}$ and $f_{2.7}$ denote the load corresponding to the drift ratio of 1.5% and 2.7%, respectively; "s" denotes the simulation; and "t" denotes test.

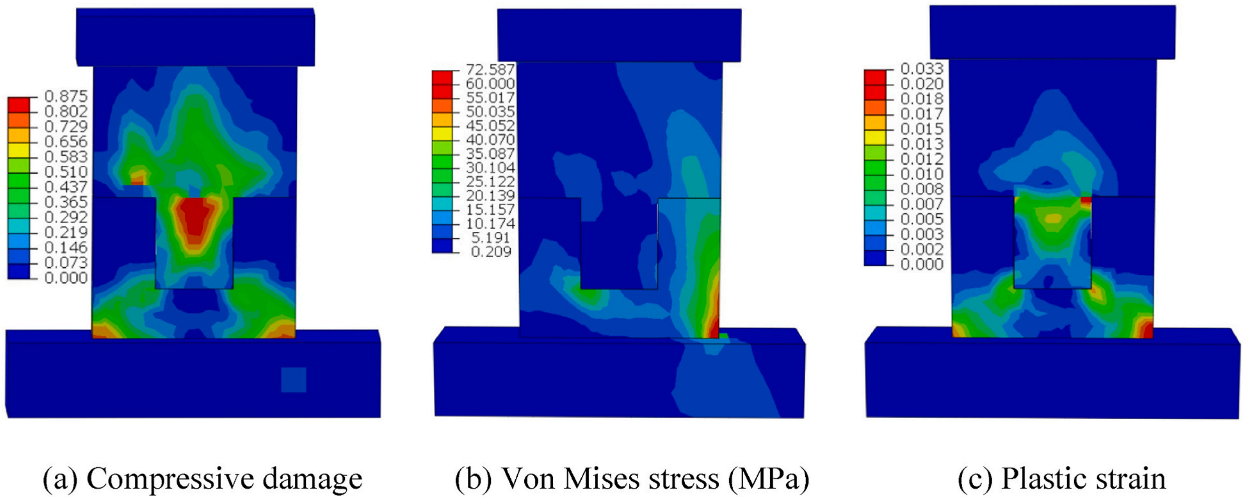

Fig. 24. Analysis results of shear wall.

matches with the experimental values, with errors within 10.3%. This result indicates that the finite element model effectively captures the cyclic behavior of the self-centering shear wall.

Fig. 24 shows the FEM results of the self-centering shear wall at a drift ratio of 2.7%, including the compressive damage, Mises stress, and plastic damage. Note that as the FEM results of SCSW1 and SCSW2 are highly similar, only the analysis results of SCSW1 are presented. The most prominent feature is the concrete damage at the replaceable corner region and normal concrete region. As a result, damage occurred during the first loading, leading to the formation of X-shaped cracks at the same location after repair, which can be seen in experimental observations in Fig. 8. In the wall corner regions where bending moments are relatively high, the UHPC effectively carries the stress in areas prone to damage, making full use of its superior mechanical properties. The maximum Mises stress at a drift ratio of 2.7% is concentrated at the wall base, which high stress can be resisted by UHPC. The plastic strain of the concrete is mainly concentrated in the lower half of the shear wall, forming an X-shaped distribution. This is attributed to the rocking mechanism of the shear wall, where stress is primarily transmitted from the wall base to the wall body once rocking occurs.

6.3. Parameter study

6.3.1. Effect of prestressing force

In the original experiment, the post-tensioned tendons in specimen SCSW1 were subjected to an initial prestress of $0.2f_{py}$. To investigate the effect of prestress levels on the self-centering behavior of the shear wall, initial prestress levels of $0.2f_{py}$, $0.3f_{py}$, and $0.5f_{py}$ were applied to the post-tensioned tendons. Fig. 25 compares the load-displacement curves and equivalent viscous damping ratio under different prestress levels. The maximum lateral load under prestress levels of $0.2f_{py}$, $0.3f_{py}$, and $0.5f_{py}$ were 441.3 kN, 549.0 kN, and 601.4 kN, respectively, representing the increases of 22.4% and 36.0% for the latter two cases compared to the first. The FEM analysis results reveal that the prestressed stress significantly enhance the shear capacity. However, Fig. 25 (b) shows that the equivalent viscous damping ratio decreases with the increase of initial prestress, indicating a gradual reduction in energy dissipation capacity. This is because higher prestress levels suppress wall cracking under low-cycle cyclic loading. An increase in the level of prestressing is associated with a corresponding increase in the degree of wall damage. Since the energy dissipation of SCSW primarily comes from wall rocking and deformation, concrete cracking, and the yielding of energy-dissipating reinforcement, the increase in initial prestress limits one of these key energy dissipation mechanisms.

6.3.2. Effect of aspect ratio

The performance of SCSWs is also influenced by the aspect ratio (h/w) of the wall. To investigate this effect, the mechanical behavior of SCSWs with aspect ratios of 1, 1.5, and 2 was studied. The width of all shear walls was kept at 1200 mm. As shown in Fig. 26, increasing the aspect ratio significantly decrease the lateral load-bearing capacity of SCSWs. The shear wall with an aspect ratio of 1 experienced rupture of the energy-dissipating reinforcement at a displacement of 19 mm, leading to the termination of the simulation. The lateral load capacities for aspect ratios of 1.0, 1.5, and 2.0 were 581.5 kN, 441.3 kN, and 383.2 kN, respectively, corresponding to a 31.8% increase and a 13.2% decrease compared to SCSW1. As shown in Fig. 26(b), reducing the aspect ratio significantly enhances the lateral load-carrying capacity and energy dissipation of the shear wall. However, it also leads to a reduction in deformation capacity. With the increase of the aspect ratio, the damage in the normal concrete region decreases, and the wall's mechanical behavior shifts from shear to flexural-dominated.

6.3.3. Effect of UHPC volume

As shown in Fig. 24 (a) and (c), the compressive damage and strain in the upper portion of the UHPC region are relatively small. Therefore, reducing the volume of UHPC can effectively lower the cost of SCSWs. In this study, two methods were employed to reduce the amount of UHPC used. The first method, referred to Ref. [58] as LessUHPC-1, involved decreasing the internal UHPC area and introducing larger chamfers within the UHPC region. The second method, named LessUHPC-2, reduced the height of the UHPC region from the original 850 mm to 550 mm. Fig. 27 compares the performance of LessUHPC-1 and LessUHPC-2 with that of SCSW1. The results indicate that both methods yielded very similar outcomes. Reducing the UHPC volume resulted in a slight decrease in the ultimate load capacity, which was measured at 400.6 kN, representing a 13.0% reduction in lateral load-bearing capacity. A moderate decline in energy dissipation capacity was also observed. However, from the observed damage distribution in the UHPC region, it is evident that the damage was primarily concentrated in the replaceable UHPC segment, while the ordinary concrete remained largely intact. This indicates a rational and efficient utilization of material properties.

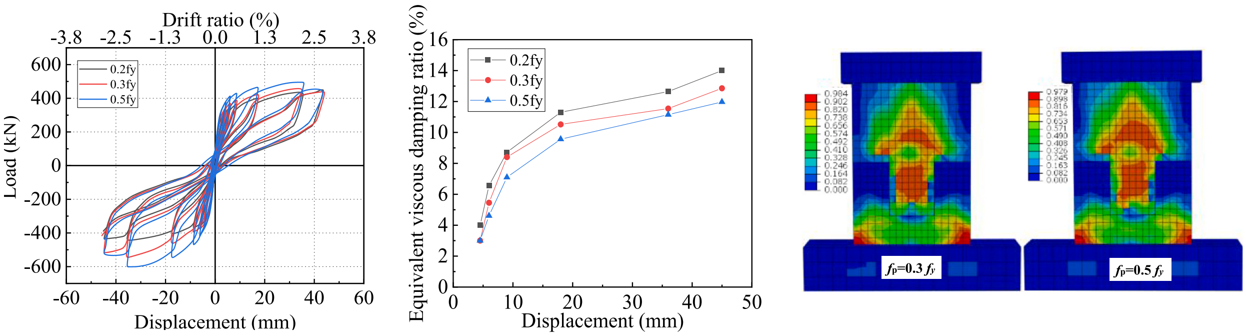

(a) Comparison of skeleton curves

(b) Comparison of equivalent viscous damping ratio

(c) Comparison of concrete damage

Fig. 25. Influences of prestressing force on SCSWs.

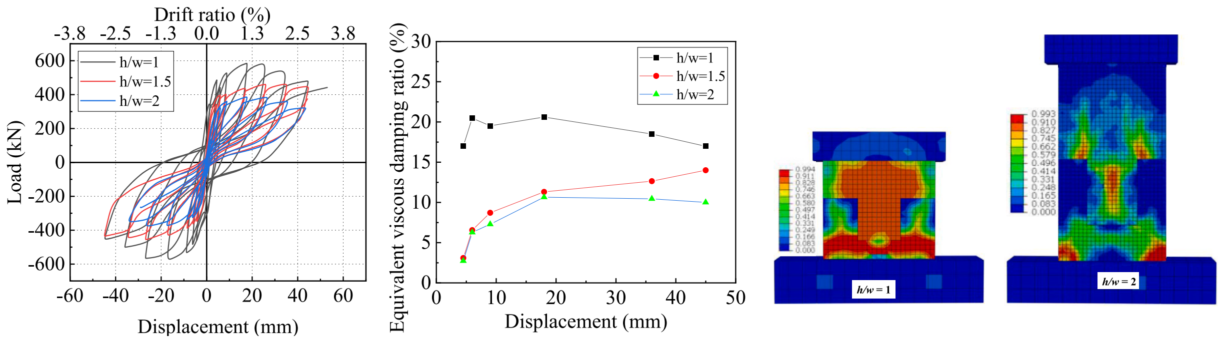

(a) Comparison of skeleton curves

(b) Comparison of equivalent viscous damping ratio

(c) Comparison of concrete damage

Fig. 26. Influences of aspect ratio on SCSWs.

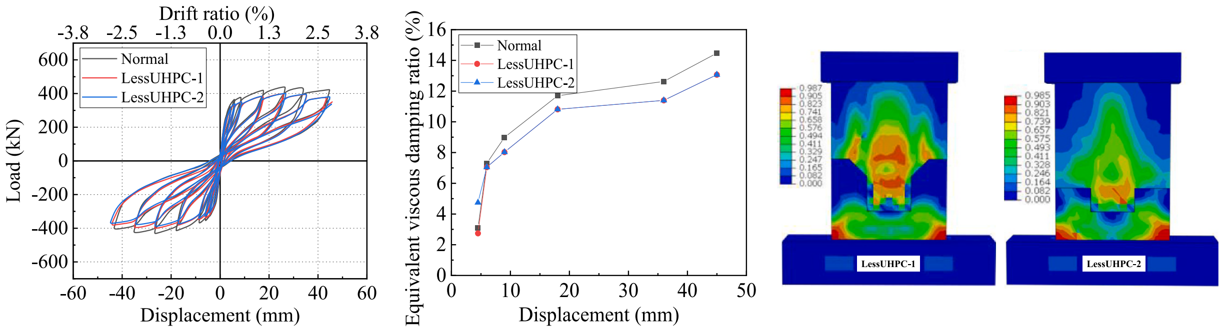

(a) Comparison of skeleton curves

(b) Comparison of equivalent viscous damping ratio

(c) Compressive damage of the two methods

Fig. 27. Influences of UHPC volume on SCSWs.

7. Conclusion

In the present study, cyclic loading tests were performed on two UHPC-based SCSWs to investigate the seismic performance. For convenient repair of damaged walls, plastic hinge regions were intentionally designed with replaceable energy-dissipation bars. UHPC was used in the corner of the wall section to reduce damage of the compression zone of the shear wall. Unbonded steel tendons and CFRP bars were used to generate the restoring force for the SCSWs. After the first cyclic loading tests, the damaged shear wall specimens were repaired and then the second cyclic loading tests were performed. The principal conclusions can be summarized as follows:

(1) The proposed SCSW specimens SCSW1 with post-tensioned steel tendons and SCSW2 with CFRP tendons exhibited similar damage patterns. SCSW1 using steel tendons developed a smaller residual displacement, indicating stronger self-centering capability. However, the energy dissipation capacity of SCSW1 was less than that of SCSW2.
(2) Compared to conventional RC shear wall SW0, SCSW1 and SCSW2 experienced less damage and the minimal residual drift (decreased by 76.2% and 54.0%, respectively), demonstrating strong self-centering capability. This result implies that SCSWs is effective for the post-earthquake structural restoration.
(3) After repair of damaged SCSWs, the seismic performance of the repaired specimens SCSW1-R and SCSW2-R exhibited similar characteristics to the counterpart specimens SCSW1 and SCSW2 in terms of failure mode, hysteretic behavior, and residual displacement. The load-carrying capacity of the repaired specimens slightly decreased by 8-10% due to the damaged wall concrete, but their equivalent viscous damping ratio was almost the same. The proposed SCSWs subjected to first and second loadings exhibited desirable earthquake resilience.

(4) The flexural strength of self-centering shear walls was calculated assuming rigid body action of the wall. The proposed model was applied to the test results of this study and existing studies. The proposed model predicted well the flexural strength of SCSWs.
(5) The FEM analysis results indicate that the SCSW wall exhibits rational load behavior. Damage and plastic strain were primarily concentrated in the replaceable region and UHPC sections, which effectively utilized the material properties and demonstrated the effectiveness of the structural design. Additionally, as the initial prestress increased, the load-carrying capacity of the SCSW wall improved, while its deformation capacity decreased. An increased aspect ratio improves the lateral load of the wall but reduce the deformation capacity. Meanwhile, a moderate reduction in UHPC volume contributes to a more rational and efficient use of materials.

In summary, the proposed SCSW demonstrates excellent seismic performance with controlled damage. The proposed detail allows for rapid post-earthquake repair while maintaining acceptable seismic performance after repair. For engineering design, initial prestress and aspect ratio should be properly controlled to balance bearing and deformation capacity, and moderate UHPC reduction in replaceable zones enables efficient material utilization. The proposed seismic resilient shear wall can be potentially used in high seismic region due to its minimal residual drift and damage repairable characteristics.

CRediT authorship contribution statement

Gao Ma: Writing – review & editing, Project administration, Investigation, Funding acquisition, Conceptualization, Validation, Supervision, Methodology. **Guoxu Zhao:** Writing – original draft, Visualization, Validation, Methodology, Formal analysis, Data curation. **Hyeon-Jong Hwang:** Writing – review & editing, Investigation, Funding acquisition.

Declaration of competing interest

The authors declare that they have no known competing financial interests or personal relationship that could have appeared to influence the work reported in this paper.

Acknowledgements

This research was sponsored by the National Natural Science Foundation of China (Grant No. 52278498 and No. 51878268), the Huxiang Youth Talent Support Program of Hunan Province, China (2021RC3041), the Natural Science Foundation of Hunan Province, China (Grant No. 2020JJ4195), and a grant (1615012983) from Digital-Based Building Construction and Safety Supervision Technology Research Program funded by Ministry of Land, Infrastructure and Transport of Korean Government. The authors gratefully acknowledge the assistance provided by Haibo He, Zewen Wang, and Guangyao Zhu for the testing.

Data availability

Data will be made available on request.

References

[1] M.N. Priestley, J.R. Tao, Seismic response of precast prestressed concrete frames with partially debonded tendons, PCI J. 38 (1) (1993) 58–69.
[2] I. Restrepo José, A. Rahman, Seismic performance of self-centering structural walls incorporating energy dissipators, J. Struct. Eng. 133 (11) (2007) 1560–1570.
[3] C. Fang, C. Qiu, W. Wang, M.S. Alam, Self-centering structures against earthquakes: a critical review, J. Earthq. Eng. 27 (15) (2023) 4354–4389.
[4] Y. Zhang, L.-H. Xu, Cyclic loading tests of a resilient hinged self-centering RC wall, Eng. Struct. 270 (2022) 114920.
[5] M. Clayton Patricia, B. Winkley Tyler, W. Berman Jeffrey, N. Lowes Laura, Experimental investigation of self-centering steel plate shear walls, J. Struct. Eng. 138 (7) (2012) 952–960.
[6] L. Xu, S. Xiao, Z. Li, Experimental investigation on the seismic behavior of a new self-centering shear wall with additional friction, J. Struct. Eng. 147 (5) (2021) 04021056.
[7] J. Wang, Z. Wang, Y. Tang, T. Liu, J. Zhang, Cyclic loading test of self-centering precast segmental unbonded posttensioned UHPFRC bridge columns, Bull. Earthq. Eng. 16 (11) (2018) 5227–5255.
[8] A. Gu, Y. Zhou, Y. Xiao, Q. Li, G. Qu, Experimental study and parameter analysis on the seismic performance of self-centering hybrid reinforced concrete shear walls, Soil Dynam. Earthq. Eng. 116 (2019) 409–420.
[9] X. Lu, X. Dang, J. Qian, Y. Zhou, H. Jiang, Experimental study of self-centering shear walls with horizontal bottom slits, J. Struct. Eng. 143 (3) (2017) 04016183.
[10] X. Du, Z. Wang, H. Liu, Numerical study of self-centering concrete wall system under cyclic loading, J. Build. Eng. 41 (2021) 102409.
[11] J. Wang, W. Zhou, Experimental and numerical response of unbonded post-tensioned rocking wall under lateral cyclic loading, J. Build. Eng. 66 (2023) 105827.
[12] Y. Zhang, L. Xu, Hysteretic behavior and parametric studies of a self-centering shear wall with tension-compression disc spring devices, Soil Dynam. Earthq. Eng. 150 (2021).
[13] Z. Zhai, W. Guo, Y. Liu, Y. Ma, F. Zhou, New precast self-centering rocking shear wall with multiple hinged joints: description and design approach for seismic protection of buildings, Eng. Struct. 262 (2022).
[14] M. ElSayed, W. El-Dakhakhni, M. Tait, Resilience evaluation of seismically detailed reinforced concrete-block shear walls for blast-risk assessment, J. Perform. Constr. Facil. 30 (4) (2016).
[15] W. Wang, J. Song, M. Hou, G. Liu, W. Wang, Experimental study and numerical simulation of replaceable corrugated steel plate-concrete composite shear walls, Soil Dynam. Earthq. Eng. 127 (2019).
[16] Y. Feng, J. Wu, X. Chong, S. Meng, Seismic lateral displacement analysis and design of an earthquake-resilient dual wall-frame system, Eng. Struct. 177 (2018) 85–102.
[17] L. Xie, X. Wang, D. Zeng, J. Jia, Q. Liu, Resilience-based retrofitting of adjacent reinforced concrete frame–shear wall buildings integrated into a common isolation system, J. Perform. Constr. Facil. 36 (1) (2022) 04021100.

[18] C. Hou, G. Ma, H.-J. Hwang, S. Li, S.-M. Kang, Seismic retrofit of intact and damaged RC columns using prefabricated steel cage-reinforced UHPC jackets and NSM GFRP bars, Eng. Struct. 317 (2024) 118665.
[19] C. Wu, G. Ma, H.-J. Hwang, Bond performance of spliced GFRP bars in pre-damaged concrete beams retrofitted with CFRP and UHPC, Eng. Struct. 292 (2023) 116523.
[20] M.J. Tolou Kian, C.A. Cruz-Noguez, Seismic design of three damage-resistant reinforced concrete shear walls detailed with self-centering reinforcement, Eng. Struct. 211 (2020) 110277.
[21] Q. Zhao, J. Zhao, J.-T. Dang, J.-W. Chen, F.-Q. Shen, Experimental investigation of shear walls using carbon fiber reinforced polymer bars under cyclic lateral loading, Eng. Struct. 191 (2019) 82–91.
[22] Y. Zhang, L.-H. Xu, Experimental investigation of a new self-centering shear wall with resilient Hinge devices, Eng. Struct. 266 (2022) 114657.
[23] Q. Liu, H. Jiang, Experimental study on a new type of earthquake resilient shear wall, Earthq. Eng. Struct. Dynam. 46 (14) (2017) 2479–2497.
[24] B. Wang, S. Zhu, Seismic behavior of self-centering reinforced concrete wall enabled by superelastic shape memory alloy bars, Bull. Earthq. Eng. 16 (1) (2018) 479–502.
[25] R. Yu, P. Spiesz, H.J.H. Brouwers, Development of an eco-friendly ultra-high performance concrete (UHPC) with efficient cement and mineral admixtures uses, Cement Concr. Compos. 55 (2015) 383–394.
[26] M.A. Bajaber, I.Y. Hakeem, UHPC evolution, development, and utilization in construction: a review, J. Mater. Res. Technol. 10 (2021) 1058–1074.
[27] M. Shafieifar, M. Farzad, A. Azizinamini, Experimental and numerical study on mechanical properties of ultra high Performance concrete (UHPC), Constr. Build. Mater. 156 (2017) 402–411.
[28] R. El-Hacha, D. Chen, Behaviour of hybrid FRP–UHPC beams subjected to static flexural loading, Compos. B Eng. 43 (2) (2012) 582–593.
[29] A.L. Hoang, E. Fehling, B. Lai, D.-K. Thai, N.V. Chau, Experimental study on structural performance of UHPC and UHPFRC columns confined with steel tube, Eng. Struct. 187 (2019) 457–477.
[30] C.-C. Hung, H. Li, H.-C. Chen, High-strength steel reinforced squat UHPFRC shear walls: cyclic behavior and design implications, Eng. Struct. 141 (2017) 59–74.
[31] X. Hu, W. Xue, Y. Lv, Seismic behavior of a new type of precast concrete shear wall using UHPC connections at boundary elements, Eng. Struct. 302 (2024) 117468.
[32] C. Wu, G. Ma, D. Zhu, H. Qu, H. Zhuang, Seismic retrofitting of GFRP-reinforced concrete columns using precast UHPC plates, Soil Dynam. Earthq. Eng. 187 (2024) 109024.
[33] S. Sharma, S. Aaleti, P. Okumus, Experimental testing of RC shear wall seismic retrofit using selective weakening, self-centering and ultra high performance concrete, Resil. Cities Struct. 2 (1) (2023) 76–90.
[34] C. Li, Y. Xiang, C. Cai, Performance of a seismic-resilient precast segmental column with UHPC segments and CFRP tendon, Eng. Struct. 282 (2023) 115833.
[35] B. Erkmen, A.E. Schultz, Self-centering behavior of unbonded, post-tensioned precast concrete shear walls, J. Earthq. Eng. 13 (7) (2009) 1047–1064.
[36] W. Wang, J. Kong, Y. Zhang, G. Chu, Y. Chen, Seismic behavior of self-centering modular panel with slit steel plate shear walls: experimental testing, J. Struct. Eng. 144 (1) (2018) 04017179.
[37] S. Basereh, P. Okumus, S. Aaleti, Reinforced-concrete shear walls retrofitted using weakening and self-centering: Numerical modeling, J. Struct. Eng. 146 (7) (2020) 04020122.
[38] C. Wu, G. Ma, H.-J. Hwang, J. Wang, S.-M. Kang, Seismic behavior of novel precast concrete shear walls with UHPC in critical areas, J. Build. Eng. 112 (2025) 113634.
[39] Concretee Structure Standard: Part 1: the Design of Concrete Structures, N.Z.S.C. Concrete, Wellington, New Zealand, 2006.
[40] A. Palermo, S. Pampanin, D. Marriott, Design, modeling, and experimental response of seismic resistant bridge piers with posttensioned dissipating connections, J. Struct. Eng. 133 (11) (2007) 1648–1661.
[41] Acceptance Criteria for Special Unbonded Post-Tensioned Precast Structural Walls Based on Validation Testing and Commentary, ACI Innovation Task Group 5: A.c. Institute, Detroit, USA, 2007.
[42] Metallic Materials - Tensile Testing - Part 1: Room Temperature Test Method, N.T.C.f.S. Standardization, Beijing, China, 2021.
[43] M.A. Mansur, M.M. Islam, Interpretation of concrete strength for nonstandard specimens, J. Mater. Civ. Eng. 14 (2) (2002) 151–155.
[44] Y. Kusumawardaningsih, E. Fehling, M. Ismail, UHPC compressive strength test specimens: cylinder or cube? Procedia Eng. 125 (2015) 1076–1080.
[45] GB50011–2010, Code for Seismic Design of Buildings, China Architecture & Building Press: M.o.H.a.U.-R.D.o.t.P.s.R.o. China, Beijing, 2010.
[46] Guide for Testing Reinforced Concrete Structural Elements Under Slowly Applied Simulated Seismic Loads, A.C. Institute, Farmington Hills, MI, USA, 2013.
[47] Y. Liu, W. Zhou, Experimental investigation of self-centering hybrid concrete shear walls subjected to horizontal cyclic loading, Earthq. Eng. Struct. Dynam. 50 (14) (2021) 3754–3770.
[48] S.-J. Xiao, L.-H. Xu, Z.-X. Li, Development and experimental verification of self-centering shear walls with disc spring devices, Eng. Struct. 213 (2020) 110622.
[49] S. Xiao, L. Xu, P. Feng, Post-earthquake performance and damage evaluation of self-centering shear wall with replaceable devices, Eng. Struct. 289 (2023) 116248.
[50] T. Hitaka, C. Matsui, Experimental study on steel shear wall with slits, J. Struct. Eng. 129 (5) (2003) 586–595.
[51] J.B. Ingo Brachmann, M. Adolfo, Drift-dependent confinement requirements for reinforced concrete columns under cyclic loading, ACI Struct. J. 101(5).
[52] R. Hassanli, M.A. ElGawady, J.E. Mills, Force–displacement behavior of unbonded post-tensioned concrete walls, Eng. Struct. 106 (2016) 495–505.
[53] M.G. Ireland, Development of a Selective Weakening Approach for the Seismic Retrofit of Reinforced Concrete Structural Walls, Civil Engineering, University of Canterbury, 2007.
[54] R.S. Henry, Self-Centering Precast Concrete Walls for Buildings in Regions with Low to High Seismicity, The University of Auckland, Auckland, New zealand, 2011.
[55] K.M. Twigden, S. Sritharan, R.S. Henry, Cyclic testing of unbonded post-tensioned concrete wall systems with and without supplemental damping, Eng. Struct. 140 (2017) 406–420.
[56] Code for Design of Concrete Structures, Ministry of Housing and Urban-Rural Development of the People's Republic of China: G, Beijing, China, 2010, pp. 50010–52010.
[57] G. Ma, J. Wang, H.-J. Hwang, O. Yang, S.-M. Kang, T. Li, Seismic performance of novel prefabricated self-centering shear walls based on UHPC, Eng. Struct. 361 (2026) 122877.
[58] L. Tiantian, Experimental and Theoretical Study on Seismic Performance of Assembled Restorable Shear Walls Based on UHPC, Hunan University, ChangSha, 2024.